Acta Materialia 243 (2023) 118543

Contents lists available at ScienceDirect

Acta Materialia

journal homepage: www.elsevier.com/locate/actamat

Effects of bridging fibers on the evolution of lamellar architecture during H_2/H_2O redox cycling of Fe-foams

Samuel Pennell *, David Dunand

Department of Materials Science & Engineering, Northwestern University, 2220 Campus Dr, Evanston, IL 60208, USA

ARTICLE INFO

Keywords:
Freeze casting
Fiber strengthening
Energy storage materials
Metals and alloys
Pore structure

ABSTRACT

Fe/Fe_3O_4 redox cycling *via* cyclic H_2/H_2O exposure at 800 °C is studied in lamellar Fe foams with 15 vol% fibers, created by freeze-casting. Fibers were integrated in the foams to mitigate densification during cycling by mechanically supporting neighboring lamellae, thus preventing buckling and sintering at contact points. Three fiber types are examined: short (0.1 mm) and long (1–2 mm) stainless-steel fibers, and long zirconia fibers. Long fibers bridge lamellae and have a marked effect on the architecture by increasing the initial interlamellar porosity (from < 60 to > 85%), with a corresponding decrease in foam shrinkage during initial reduction and sintering (from > 80 to < 55% volumetric loss). Though performance improves as compared to fiber-free foams, fiber effectiveness against damage decreases with cycling: after 10 redox cycles, porosity falls from 85 to 50% for foams with long fibers. One novel degradation mechanism is identified: fiber engulfment. This mechanism occurs over successive redox cycles, as material from the lamellae cyclically engulfs (as Fe_3O_4) and withdraws (as Fe) from the fibers, with a net transport from lamellae to fibers after each cycle. This cyclic coarsening mechanism alters foam architecture from bridged-lamellar (with evenly distributed porosity) to mixed lamellar/fibrous (with unevenly distributed porosity).

1. Introduction

Freeze-casting is a facile and inexpensive means of introducing controllable, oriented porosity into a wide variety of materials systems [1,2]. In brief, a thermal gradient is applied to a slurry, inducing solidification along the gradient direction. As the solidification front moves, solid dendrites can either engulf or reject the solid content of the slurry. If solidification velocity is higher (respectively, lower) than a critical velocity v_c, which can be calculated from the nominal particle size and slurry viscosity, suspended particles are rejected (respectively, engulfed) by the solidification front [3]. Together with the freezing velocity, the liquid used (and its structure when solidified), as well as the nature and amount of additives (e.g., binder, dispersant) also play an important role in determining the final freeze cast structure. In particular, water is typically freeze-cast into lamellar structures owing to the hexagonal crystal structure of water ice, which allows ice dendrites with favorable orientation to grow preferentially along the thermal gradient. The shape of these lamellar ice dendrites may be altered, for example by the addition of gelatin, which introduces additional connectivity between lamellae to form an architecture consisting of interconnected elongated cells [4]. A group of neighboring lamellae with a shared orientation is referred to as a colony, expected to have formed from aligned dendrites within a single grain of ice during freeze-casting; a single foam consists of multiple colonies, with the number and size of colonies dependent on the how many ice grain nucleated at the bottom of the sample during the freeze casting process. Each lamella typically spans the width of its colony, and connects to lamellae in neighboring colonies.

The lamellar architecture created when particles are rejected from growing ice dendrites consists of alternating pure ice lamellar dendrites and particle/ice interdendritic lamellar volume, ~10 μm in width for common freezing velocities. Once the ice is sublimated and the particles are sintered in their templated architecture, the resulting lamellar porous materials have various structural applications (e.g., bone scaffolds and aerospace load-bearing components), as well as functional applications (e.g., filters, wicks, electrodes, and gas reactors) [5–7]. We focus here on the performance of freeze-cast, lamellar Fe architectures during gas redox reactions, as interlamellar channels provide both steady gas flow and accommodation for lamellar expansion during oxidation, thus maintaining high surface area for the reaction.

* Corresponding author.
E-mail address: samuelpennell2024@u.northwestern.edu (S. Pennell).

https://doi.org/10.1016/j.actamat.2022.118543
Received 28 September 2022; Received in revised form 18 November 2022; Accepted 19 November 2022
Available online 20 November 2022
1359-6454/© 2022 Acta Materialia Inc. Published by Elsevier Ltd. All rights reserved.

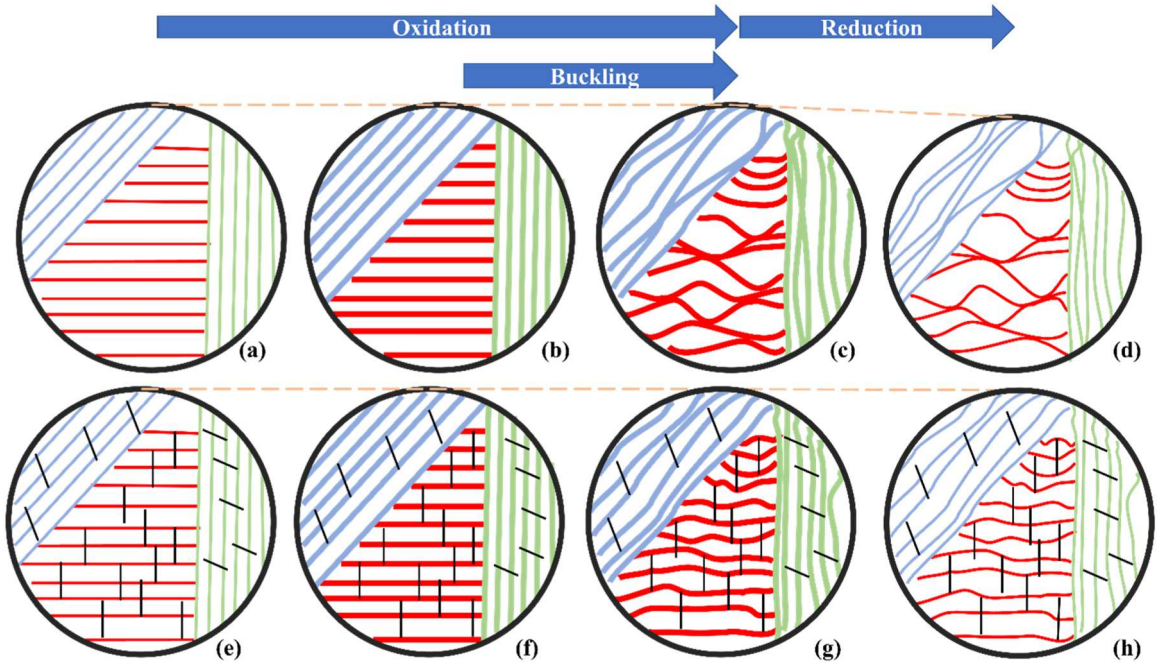

Fig. 1. Schematic depiction of lamellar buckling during redox cycling of (a–d) fiber-free and (e–h) fiber-containing foams, shown in a radial cross-sections with three lamellar colonies. (b, f) Oxidation causes a volumetric increase for each lamella. (c, g) This induces in-plane compressive stresses in lamellae, causing lateral deflections via buckling which puts neighboring lamellae in contact, with sintering occurring at contact points (for clarity, oxidation and buckling are depicted in separate steps, but these processes occur simultaneously). (d, h) After reduction, these contact points remain sintered, and buckling is not reversed, causing a net shrinkage in the foam without fibers (orange dashed line). For fiber-containing foams, the fibers support lamellae laterally, limiting the amplitude of buckling induced during oxidation, and thus reducing contact points and subsequent lamellar sintering.

To increase the strength and stiffness of lamellar freeze-cast ceramic foams, bridges can be introduced between lamellae to provide support against lateral deflection (buckling) occurring when the foam are deformed in uniaxial compressive mode [8–11]. Bridging techniques include both *in-situ* methods (e.g., inducing bridge growth during solidification by increasing binder content of the slurry [12–15]) or *ex-situ* methods (e.g., adding fibers [8–10] or platelets [16] which bridge freeze-cast lamellae). These bridging strategies reduce lamellar buckling by adding rigid connectors preventing lateral deformation of the lamellae. Here, we explore the use of fiber bridging to mitigate internal lamellar deformation in a functional material subjected to internal swelling from redox reactions, rather than a structural component subjected to external forces.

For iron-based redox systems, the lamellar freeze-cast architecture presents a morphological alternative to commonly used packed-powder beds. Redox systems are relevant for H_2 production and storage; when paired with a reversible solid-oxide fuel cell, they can operate as reversible iron-air batteries [17–21]. The natural abundance, very low cost, and ecologically benign character of iron and its oxides are attractive for large-scale energy storage. In these Fe-based systems, during discharge, metallic Fe is oxidized by steam to Fe_3O_4 and H_2 is liberated by the following reaction:

$$Fe + H_2O \rightarrow FeO + H_2 \quad (1a)$$

$$3FeO + H_2O \rightarrow Fe_3O_4 + H_2 \quad (1b)$$

During charging, H_2 reduction of Fe_3O_4 forms Fe, with the above reactions being reversed. The very large $Fe \rightarrow Fe_3O_4$ molar volume expansion (110%) incurred upon oxidation leads to sintering of the Fe lamellae, and thus loss of performance, by reducing the surface to volume ratio of the Fe lamellae in the foam, and thus increasing the diffusion distance needed to drive the diffusion-dependent oxidation and reduction reactions, as reported in Fe-foam systems [22] and in Fe-powder bed systems [23–27]. For example, a study by Otsuka et al. [26] showed that, between the first and second redox cycles, a four-fold increase in oxidation time was needed to produce equivalent volume of H_2 gas, for samples with initially relatively high specific surface area ($20\ m^2\ g^{-1}$).

As compared to powder bed geometries, a lamellar Fe-foam architecture prolongs the number of redox cycles with comparable kinetics [22]. These lamellar foams, however, still undergo densification, which kinetically limit the redox reactions by choking access to gasses and increasing diffusion distances. Lamellar densification is driven by several interrelated mechanisms that decrease the mean distance between lamella, leading to lamellar contact, sintering, and densification: (i) lamellar buckling; (ii) Kirkendall pore nucleation and growth; and (iii) lamellar tip splitting and sintering [22,28]. Buckling of Fe lamellae is an important damage mechanism, as it lead to contact and sintering between neighboring lamellae, and thus loss of channel porosity and overall foam densification, reducing the access of gas and decreasing the surface-to-volume ratio of the active material [22,28–34].

The buckling of lamellae in the Fe redox foams occurs as the volume increase associated with oxidation generates compressive internal stresses in the plane of each lamella as it is partially prevented to expand longitudinally because of neighboring colonies. A simplified, two-dimensional schematic illustrating lamellar buckling during redox cycling is shown in Fig. 1, along with the hypothesized effects of fiber bridges on lamellar buckling. The foam initially consists of three colonies of lamellae (Fig. 1a,e). As oxidation causes each lamella to increase its volume (Fig. 1b,f), lamellae can freely expand in directions perpendicular to the lamellar planes, by thickening into the free space of the channel. However, expansion is constrained in directions within the lamellar plane, as the edges of each lamella impinges on neighboring lamellar colonies, thus inducing internal compressive stresses that cause buckling (Fig. 1c,g). For clarity, oxidation and buckling are depicted in separate schematics; however, these processes occur simultaneously. Severe buckling leads to contact and irreversible sintering between neighboring lamellae within colonies; during reduction, the volume

contraction then leads to a net shrinkage of the foam (Fig. 1d). Fibers bridging adjacent lamellae are expected to act as perpendicular supports, reducing the buckling amplitude by limiting the length of unsupported lamellar segments.

The buckling of lamellae in freeze-cast foams due to redox cycling, and the effects of fiber bridging on the buckling, is a complex process since the lamellae: (i) have pre-existing curvature (formed during initial powder reduction and sintering during foam fabrication), (ii) comprise both oxide and metallic regions, whose fractions evolve during oxidation, (iii) undergo buckling via both creep-controlled and elastoplastic mechanisms, and (iv) buckle in three dimensions, given the multiaxial state of internal stress. Research is ongoing in developing a finite-element model that accounts for these factors and describes the buckling evolution in more detail.

Bridges produced *in situ* were previously studied in the context of redox cycling, with the conclusion that the bridges negatively impacted cycling performance by increasing contact points between neighboring lamellae, leading to increased sintering, coarsening, and significantly reduced open porosity [35]. Thus, while buckling was mitigated, performance suffered overall due to the coarsening of the bridges, since they were composed of the same redox-active material as the lamellae.

In this work we introduce in the lamellar Fe foams three types of fibers with various lengths and compositions, thus creating Fe-based foams with a mixed lamellar/fibrous architecture. We study the chemical and mechanical interactions between the Fe-lamellae and the fibers during redox cycling, when the phase change creates large volume expansion and contractions, both for fibers which are partially soluble (metallic fibers) and fully insoluble (oxide fibers).

2. Experimental procedures

2.1. Freeze casting and sintering of fiber-containing Fe foams

Lamellar foams with 10 vol% solid content (with a Fe/fiber volume ratio of 85/15 after reduction) were fabricated by directional freeze casting. Three fiber types were used: 316 L stainless steel fibers (Fe-18Cr-10Ni wt%) with (i) short length (75–100 μm length, 2–3 μm diameter, from Bekaert Corporation, Zwevegem, Belgium), and (ii) long length (1–2 mm length, 6–9 μm diameter, from Stanford Advanced Materials, Lake Forest, CA), and (iii) yttria-stabilized zirconia (YSZ) fibers (ZYBF-5, from Zircar Zirconia Inc., Florida, NY) with long length (1–2 mm length, 6–9 μm diameter).

Because the steel fibers have high density, preventing their settling is a significant challenge. It is addressed by employing a mixed gelation-freeze-casting strategy. First, 3.5 g Fe_2O_3 powders (SkySpring Nanomaterials, Houston, TX, USA) were mixed with 3 mL DI water and 0.07 g Zephrym PD as dispersant. This slurry was ball milled for 48 h in a rotary mill with zirconia milling ball media (equal volume of media to slurry). Separately, 0.3 g steel fibers were sieved through a 45 μm sieve to limit fiber clumping. These were mixed with 3 mL DI water, 0.04 g PEI as surfactant, and HNO_3 was added dropwise to achieve a pH of 4. This suspension was heated to 100 °C, 0.15 g agar powder (NOW Real Food, Bloomingdale, IL) was added and dissolved by stirring, and then mixed by hand with the ball-milled Fe_2O_3 slurry. Next, 0.26 g isopropyl alcohol was added to lower the slurry viscosity (and thus increase lamellar spacing after solidification [36]). The mixed slurry was degassed under vacuum, placed in an ice-water bath to cool it to 1 °C, and finally freeze-cast under directional conditions. Control fiber-free foams added were prepared by the same method, to assess the effects of the gelling agent on freeze-cast architecture.

The YSZ fibers, which have a lower density than stainless steel, do not require the gel-casting process to produce a stable slurry. Instead, 3.5 g Fe_2O_3 powders (SkySpring Nanomaterials) were mixed with 3 mL DI water and 0.07 g Zephrym PD as dispersant. This slurry was ball milled under the same conditions. Separately, 0.15 g YSZ fibers were added to 3 mL DI water with 0.12 g PEG as binder. After milling, the two suspensions were processed with the same steps as outlined above, before freeze casting.

Directional freeze-casting was carried out in a cylindrical Teflon mold (15 mm ID, 26 mm OD, 15 mm height) placed on a copper plate and insulated with a Styrofoam sleeve. The copper plate was cooled by a thermoelectric cooling device (Mauser Technologies) to 0 °C before casting. After the 1 °C slurry had been poured into the mold, it was cooled in an exponential cooling curve from 0 to −30 °C to ensure a constant freezing velocity of 16 μm/s, as reported elsewhere [33,37].

The lowest 1 mm portion of the frozen specimens, which had been in contact with the Cu plate and had not yet formed a uniform lamellar structure, was removed with a razor blade. The samples were then freeze-dried for 48 h in a Labconco dryer at −22 °C and 0.13 mbar vacuum to achieve full ice sublimation. The ice-free green bodies were placed in an alumina tube furnace (42 mm ID, 50 mm OD, 700 mm length) and held at 300 °C for 1 h in flowing H_2 (99.999% pure, Airgas) to remove binder and dispersant. In the same gas environment, the Fe_2O_3 was then reduced at 600 °C for 4 h and the resulting Fe lamellae (with their fibers) were sintered at 1000 °C for 3.5 h, with heating and cooling rates of 10 and 5 °C/min, respectively.

2.2. Redox cycling

Redox cycling was performed using alternative flows of H_2- and H_2O-rich gasses in an alumina tube furnace (19 mm ID, 25 mm OD, 610 mm length). Cycling was performed at 800 °C, a higher temperature than most operating iron-air battery temperatures, to accelerate the redox reactions and enhance microstructural and macrostructural changes that may occur at lower temperatures, so as to reduce the number of cycles needed to assess the damage resistance of the foams. Initially, each foam, positioned on an alumina plate, was heated to 800 °C at 10 °C/min under a 100 sccm flow of H_2 (99.999% pure, Airgas). The 60 min oxidation half-cycle was conducted under a 120 sccm flow of steam-saturated Ar, created by flowing Ar (99.999% pure, Airgas) through a water bubbler held a 93 °C (to achieve a H_2O partial pressure of 0.77 atm). The subsequent 90 min reduction half-cycle again used pure H_2 (200 sccm). After one or more such redox cycles, the samples were cooled at 10 °C/min under flowing H_2 (100 sccm) when ending at the end of a reduction full-cycle step. When ending during a partial oxidation or reduction half cycle, foams were instead cooled under Ar-4%H_2 (20 sccm, Airgas) to minimize oxidation or reduction during cooling. Foam dimensions and mass were measured before and after cycling, with mass change used to confirm full conversion between Fe and Fe_3O_4 for the above cycle times.

Foams were vacuum-mounted in epoxy (Epothin 2, Buehler), ground on a rotating wheel to roughly halfway through the sample height, and polished *via* standard metallographic procedures, with the final step using a 1 μm diamond suspension. Foam radial cross-sections were optically imaged (Nikon Eclipse MA200, Wild M3Z Stereoscope), and ImageJ was used to derive microstructural parameters. An image of the entire radial cross section (perpendicular to the solidification direction), created by stitching low-magnification optical micrographs, was converted to binary pixels assigned to lamellae, fibers, and epoxy background (channel volume). These slices were then processed by twice applying a median filter (radius of 3 pixels) to exclude micropores within lamellae. Channel volume fraction (i.e., foam porosity) was then calculated from the lamellar volume fraction, taken as the ratio of the void pore area to the total area within the outline of the foam. The ImageJ plugin “Local Thickness” was applied to the filtered image to calculate both lamellar wall thickness and channel thickness [38]. Previous tomography studies have confirmed that these measurements on 2D slices are representative of bulk foams [32]. Imaging *via* scanning electron microscopy (SEM) and electron diffraction spectroscopy (EDS) was performed with a Hitachi 8030, under 15 kV accelerating voltage and 10 μA probe current, on mounted, polished foams, which were sputter-coated with a 10 nm Au-Pd film.

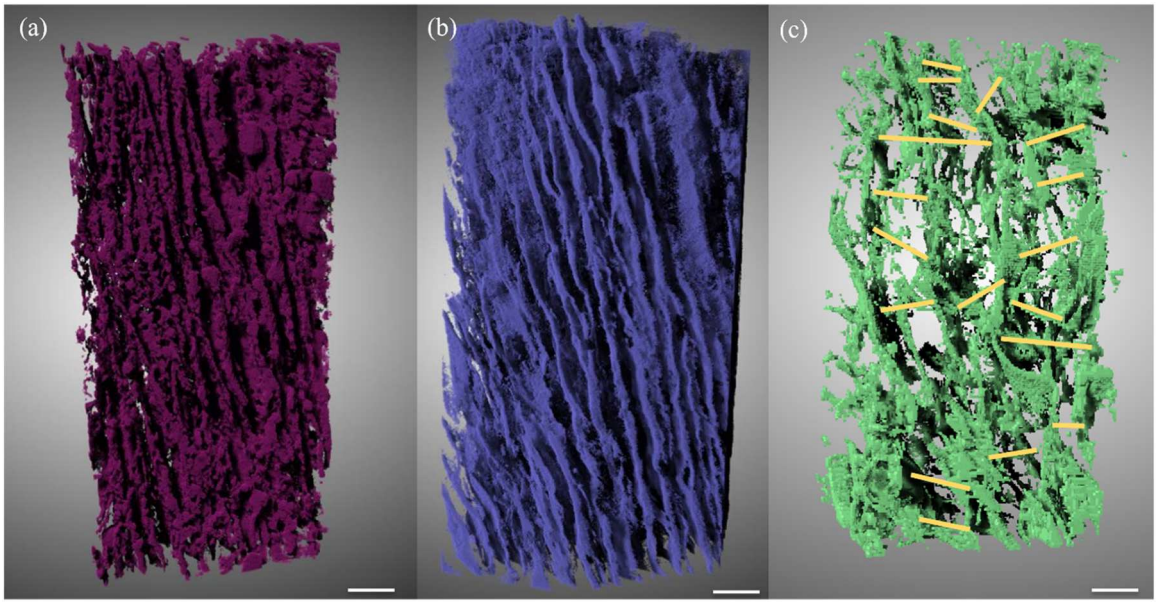

Fig. 2. Tomographic reconstructions of as-fabricated Fe foams (a) without fibers (control); (b) with short steel fibers; and (c) with long steel fibers. Scale bar marks 100 μm To guide the eye, long steel fibers in (c) are marked with yellow lines.

2.3. X-ray microtomography

X-ray microtomography was conducted at Sector 5-BM of the Advanced Photon Source (APS, at Argonne National Laboratory, IL, USA). Specimens measuring $3 \times 3 \times 4$ mm^3 or $1 \times 1 \times 2$ mm^3 (for voxel size of 6 or 2.4 μm, respectively) were sectioned from epoxy-mounted samples. The larger voxel size was used for the Fe foams with long steel fibers, and the smaller voxel size was used for the foams with short steel fibers and without fibers. Tomography was not performed for a foam with long YSZ-fibers, due to beam access limitations.

Tomographic reconstructions were performed with Dragonfly ORS software and ImageJ software. The different dimensionality of lamellae and fibers were used to segment these features for the long steel fibers; the small size of the short steel fibers made them unresolvable for the voxel size used. The segmentation relied on the assumption that lamellae have significantly longer dimension along the z-axis, in the direction of freezing. By mapping the volume thickness of the reconstruction and applying an Otsu threshold to the resultant map, the lamellae could be distinguished from the fibers. The Otsu filter removed the bulk of the lamellar volume except for edges of lamellae, because they have less z-axis volume, which were subsequently removed by filtering voxels with fewer than 8 neighbors. Intersections between fibers and lamellae were also removed, so the analysis could be performed on the segments of fibers spanning channels. After separating the fibers from the lamellae, skeletonization was performed in ImageJ to collect orientation and position information on the fiber segments.

3. Results and discussion

3.1. Freeze-cast architecture

3.1.1. Foam architecture

The effects of fibers on the architecture of freeze-cast Fe foams were explored by tomographic reconstruction of representative sections for each sample type. Reconstructions after initial sintering (before redox cycling is performed) are shown in Fig. 2(a–c). The control, fiber-free foam (Fig. 2a) shows characteristic lamellar structure, with well-aligned Fe lamellae separated by channels with uniform thickness, in agreement with previous studies [22,28–33]. Thus, the addition of the gelling agent does not significantly alter the freeze-cast structure for the Fe control samples. The addition of short fibers does not greatly alter this architecture (Fig. 2b); the lamellae remain well aligned and the channels have uniform width, whose average width is however larger than in the control sample. Due to the small dimensions of the short steel fibers, they could not be resolved by tomographic reconstruction.

The foam with long steel fibers (Fig. 2c) shows a significantly altered architecture. Although the lamellae are generally oriented in the freezing direction, they are less well aligned than for the other two specimens (Fig. 2(a,b)). We hypothesize that this altered architecture is induced by the fibers during reduction and sintering. Because the fibers pin the lamellae at intersection points, the movement of the lamellae is constrained as they shrink during the reduction and sintering process, resulting in local (rather than large-scale) changes in lamellar alignment after reduction and sintering. That these changes are not observed for the short-fiber sample is consistent with the expected lesser ability of short fibers to prevent buckling of lamellae. Although this produces additional tortuosity in the channels, it is not expected to markedly alter the diffusion of the reducing or oxidizing gasses into the foam, as the channels are still fully open and the lamellae are not wider than in the other foams.

3.1.2. Foam shrinkage and colony orientation

In the foam with long steel fibers (Fig. 2c), channels are much wider (after reduction and sintering), and the sample is correspondingly more porous than the short-fiber foam (Fig. 2b) or the control foam (Fig. 2a). This is consistent with the long fibers preventing lamellar buckling and the associated contact between and sintering of neighboring lamellae. A previous study by Wilke et al. [34] detailed the evolution of lamellae as the Fe-foam undergoes a large volumetric shrinkage, mainly stemming from the large molar volume change associated with the reduction of Fe_2O_3 to Fe. This volume change causes lamellae to buckle within each colony, due to stresses incurred from neighboring lamellar colonies, which narrows the channels between neighboring lamellae as lamellae merge. If fibers are present, however, this buckling and the resulting lamellar merging are mitigated, as shown by the strong decrease in volumetric shrinkage exhibited by fiber-containing samples: from ~85% for Fe, to ~70% for the short-fiber foam, to ~40–50% for the two long-fiber foams (as shown graphically in SI Fig. 1). Thus, both fiber sizes have a strong effect, but the long fibers have the strongest sintering inhibition, likely because they are both more likely to fully bridge

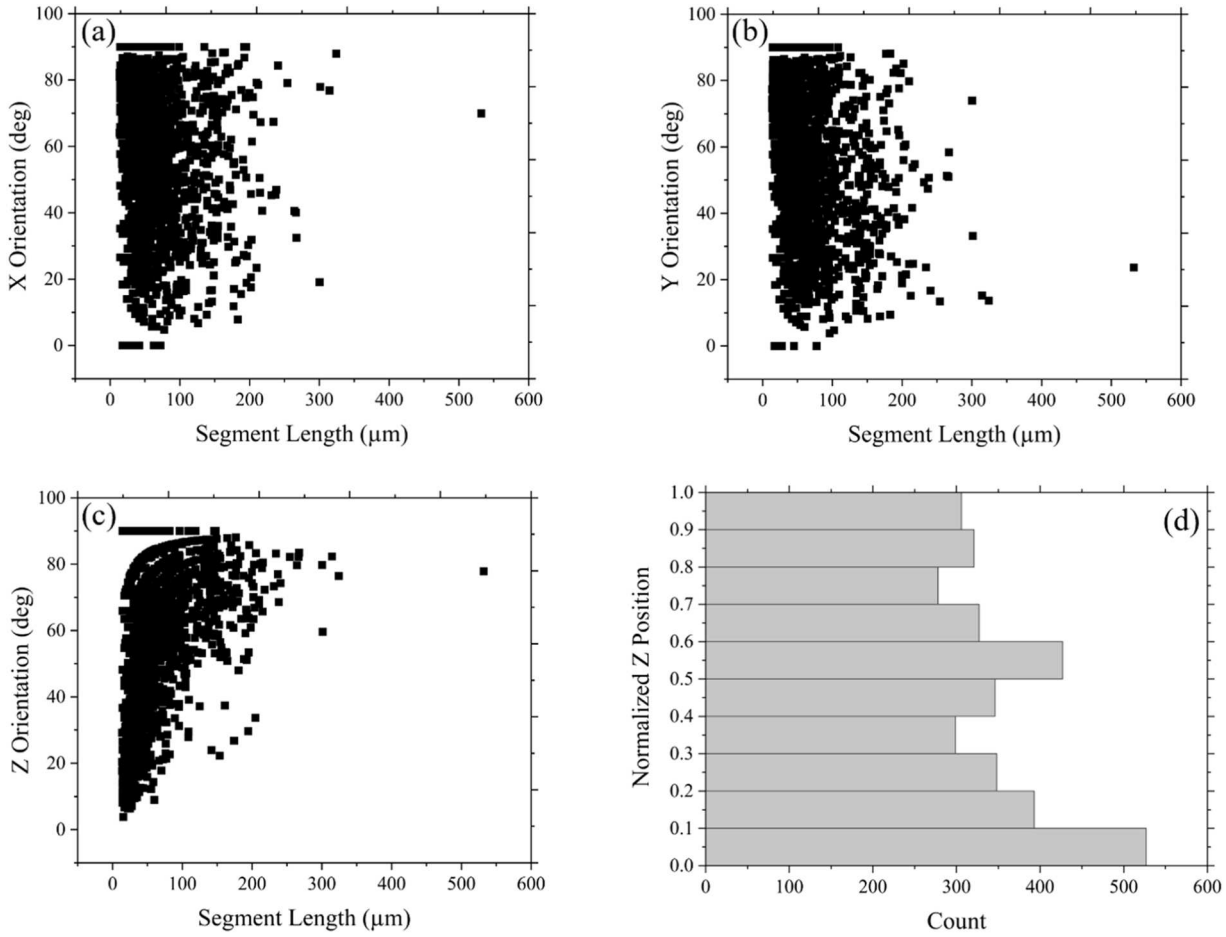

Fig. 3. Plots of (a–c) fiber orientation and (d) fiber position within Fe foam height, as determined from tomographic reconstruction of an as-fabricated foam with long steel fibers. In (a–c), the orientation of fiber segments with respect to the x-, y- and z-axes, respectively, is plotted against their length. The data-free zone between 75 and 90° in (c) is an artefact: for these short fibers, there is a limited number of possible orientations in which the voxels can occur with respect to each other. In (d), fiber number is plotted against the normalized z-position of fiber (defined as the center of each fiber segment) over the reconstructed foam segment normalized height.

channels and less likely to buckle themselves, due to their increased diameter, as discussed in more details in later sections.

The large gaps between colonies observed for large fiber-containing foams can also be explained by the mitigation of shrinkage. Because the movement of each lamella is constrained, the net shrinkage of the sample is limited; this results in preservation of wider channels between lamellae, and preservation of wider gaps between colonies. The effects of these wide inter-colony gaps are explored further in Section 3.2.

3.1.3. Fiber orientation and distribution

To assess fiber performance, fiber segments were identified into three types: (i) type-I segments, which completely bridge the channel between two neighboring lamellae, (ii) type-II segments, which have both segment ends embedded in the same lamella, and (iii) type-III segments, which lie partway across channels. Only type-I bridges are expected to contribute to mechanical support between lamellae.

The position and orientation of fibers, which will affect anti-buckling performance in the bulk foams, are reported in Fig. 3 for foams with long steel fibers after reduction and sintering. Fig. 3(a,b) show the orientation of fiber segments with respect to the x- and y- axes, respectively, which define a plane perpendicular to the freezing direction. These plots show a near-random distribution, as expected if the fibers are suspended in the freezing liquid with no preferred orientation. In Fig. 3(c), the fiber segment orientation is shown with respect to the z-axis (freezing direction): many more fibers are close to perpendicular to the freezing direction (between 70 and 90°), and the distribution smoothly decreases with decreasing angle, indicating that fibers are bridging lamellae as intended. Fig. 3(d) indicates that the fibers are distributed over the full height of the foam, with some sedimentation occurring in the bottom 10% of the foam.

3.1.4. Fiber bridges

While skeletonization is effective in mapping the positions of the nearly one-dimensional fibers, determining their position with respect to the lamellae requires additional information. To accomplish this, foams were examined in SEM without metallographic preparation . Because of the depth of field afforded by SEM imaging, bridges were classified both at the sample exterior and as far into the foam as could be observed without cutting the foam. Representative micrographs and bridge counts for each sample type are shown in Fig. 4. As expected from their shorter length, the short steel fibers exhibit by 2–3 time more type-III fiber segments than the long-fiber foams (steel and YSZ), decreasing their anti-buckling effectiveness. By contrast, for both long-fiber foams, ~ 70% of observed bridges are classified as type-I. The higher proportion of type-III bridges observed for the long YSZ fibers as compared to the long steel fibers (15 and 10%, respectively) is likely due to fiber fracture during reduction and sintering, as the brittle YSZ fibers forming type-I and -II bridges fracture during foam shrinkage, thus becoming type-III bridges.

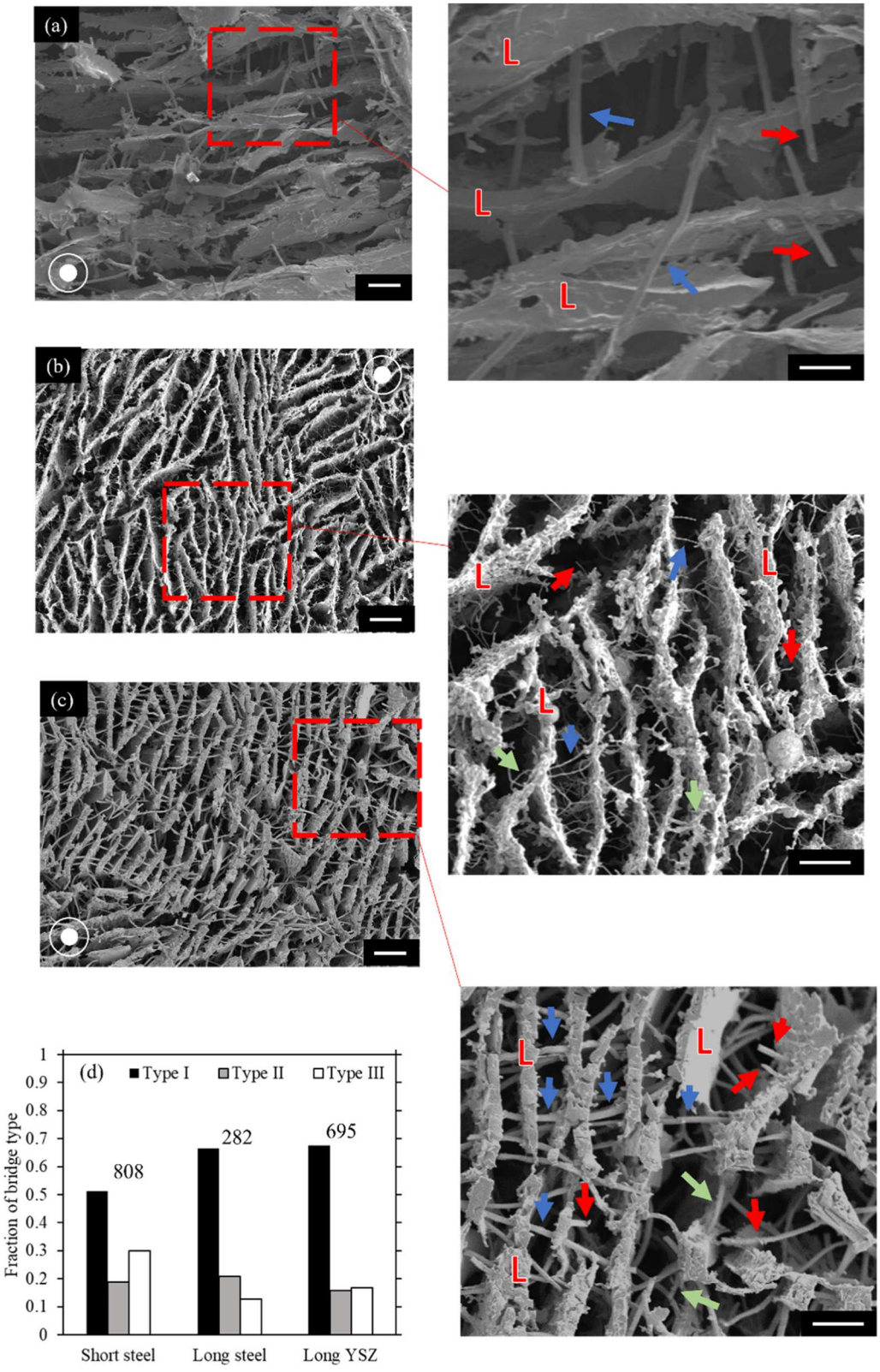

Fig. 4. SEM micrographs of foam surfaces, showing characteristic bridged lamellar regions of as-fabricated Fe foams with (a) long steel fibers, (b) short steel fibers, and (c) long YSZ fibers, showing Fe lamellae bridged by fibers (scale bar marks 100 μm). Insets show higher magnification views (scale bar marks 50 μm), with examples of type-I bridges marked by blue arrows, type-II bridges by green arrows, and type-III bridges by red arrows; some of the lamellae are marked with "L". Freeze cast direction indicated in white. (d) bar graph showing fraction of each bridge type for the three foams in (a-c), with total number of fiber segments marked above each bar cluster.

3.2. Redox cycling

3.2.1. Channel porosity and channel thickness

The interactions between Fe lamellae and fibers during redox cycling varies depending on fiber type. In all cases, however, foam densification occurs with repeated cycling, reducing foam porosity and channel thickness, while also increasing lamellar thickness. Trends for these three microstructural features, over 10 redox cycles, are shown in Fig. 5 (a,b). When comparing, in these figures, with data for fiber-free Fe-foams, it is apparent that fibers provide a significant improvement in resistance against densification, stemming from higher initial values of porosity (80–90% for the three fiber-containing foams, vs. ~ 60% for the

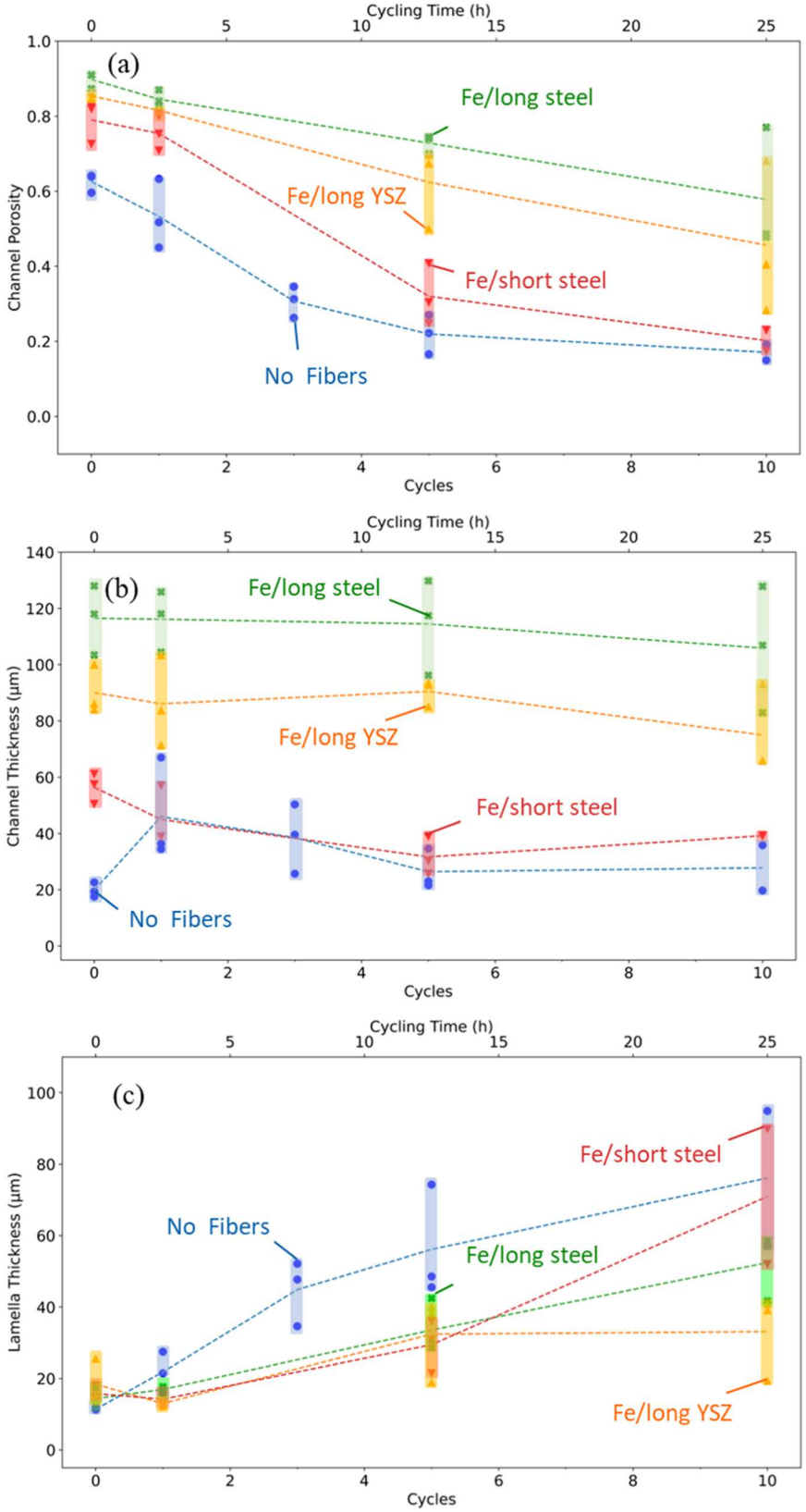

Fig. 5. Evolution with redox cycling of (a) channel porosity, (b) channel thickness, and (c) lamella thickness for Fe foams with long steel fibers (pink), long YSZ fibers (black), short steel fibers (blue); for comparison, data (red, from [29]) are also shown for fiber-free Fe foams.

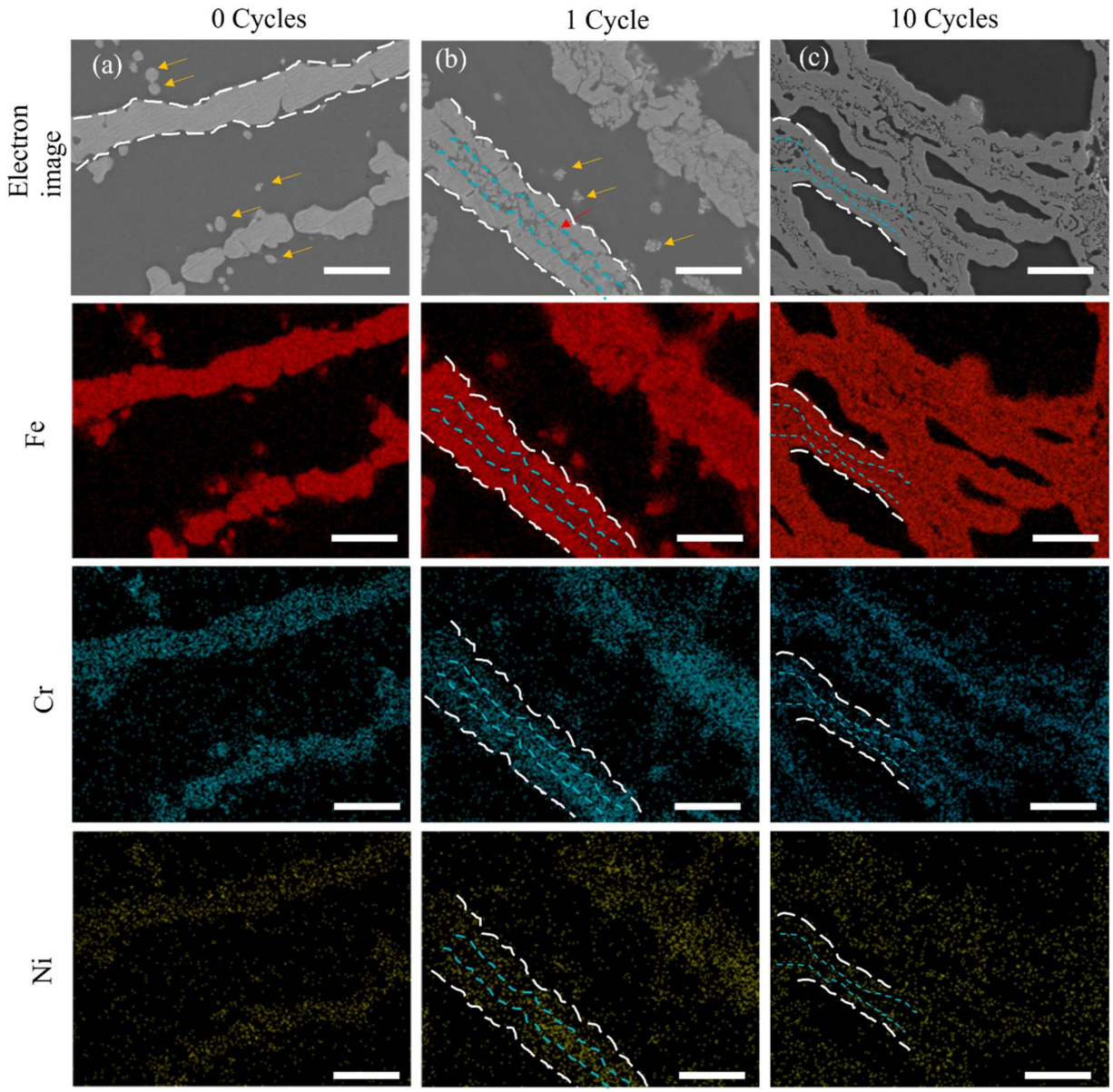

Fig. 6. Radial SEM micrographs showing cross sections of lamellae for Fe foam with short steel fibers, with corresponding EDS maps of Fe, Cr, and Ni, showing microstructural evolution after (a) 0 redox cycles (as sintered) with Ni and Cr present in the lamellae, after diffusion from the fibers during foam processing, (b) 1 redox cycle, and (c) 10 redox cycles, with metallic Ni and oxidized Cr in the lamellar cores. The red arrow in pane (b) marks delamination between the Cr_2O_3-rich core and the Fe-rich shell. Yellow arrows mark fiber cross sections. White and blue dotted lines guide the eye for lamellar edges and cores, respectively. Scale bar marks 10 μm.

fiber-free Fe foam) and channel thickness (90–120 μm for long-fiber foams, ~60 μm for short-fiber foams, and ~20 μm for fiber-free foams). For the short-fiber foams, the benefit of an initially higher porosity disappears after 5 redox cycles, as the short steel fibers are rapidly engulfed during cycling (as discussed in Section 3.2.4), losing their efficacy. Foams with long fibers, however, provide a longer-lasting resistance against sintering during redox cycling: after 10 cycles, foams with long steel and long YSZ fibers have mean channel porosities of 46–48%, far above the 17% value for fiber-free Fe foams. These results also indicate that bridging via fiber additions is a more effective strategy for preserving porosity than bridges formed *in situ* during freeze casting, as previous work showed that foams with *in situ* bridges densified rapidly, e.g. to 15% porosity after only 5 cycles [35].

Foam sintering due to buckling can be quantified by measuring the average lamella thickness, as shown in Fig. 5c after 10 redox cycles; this is because the volume loss of foams undergoing sintering is driven by neighboring lamellae contacting and sintering together, thus forming fewer, wider lamellae after their merger. For fiber-free foams, lamella thickness increases strongly, from 11 to 76 μm in 10 cycles. Foams with short fibers show a similar strong increase due to ineffective buckling mitigation, from 15 to 71 μm. Foams with long steel fibers show less sintering, with a lesser increase in lamellar thickness, from 15 to 50 μm. Foams with long YSZ fibers show the best sintering prevention, with lamella thickness increasing from 18 to just 33 μm in 10 cycles.

Overall, foams with long steel and long YSZ fibers perform similarly to each other over 10 redox cycles, implying that the size of the fiber is more consequential than the material of the fiber (at least for fiber materials able of withstanding the cycling conditions without disintegrating). For facile processing, the less dense YSZ fibers are a better choice, as their sedimentation during freeze casting is more easily avoided.

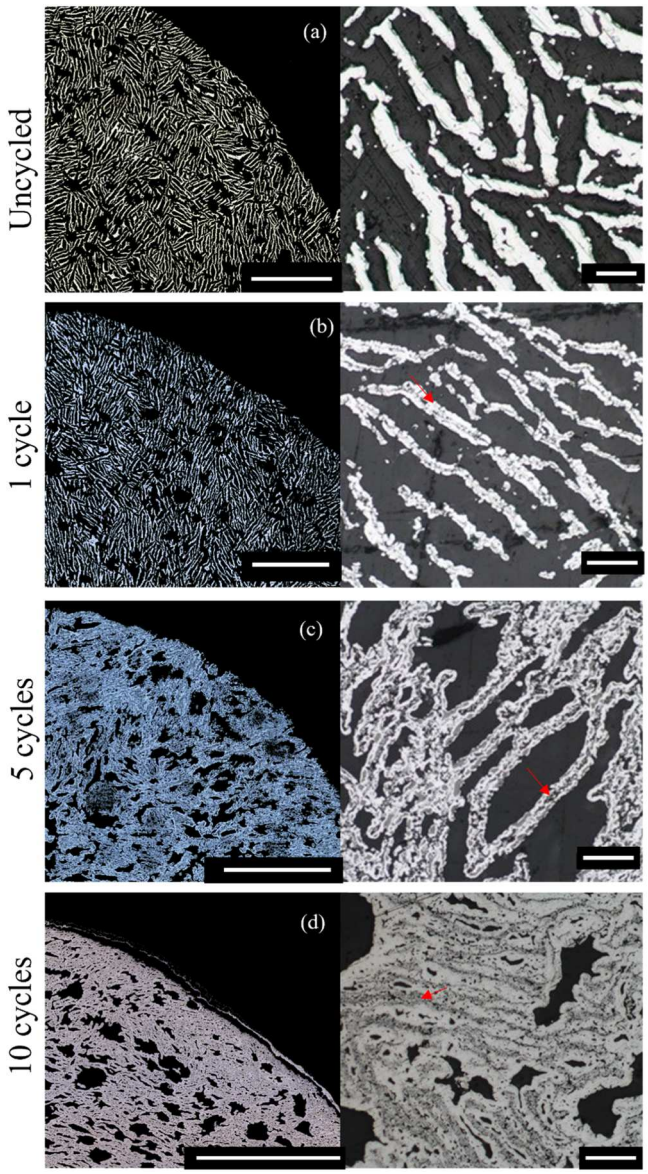

Fig. 7. Optical micrographs of radial cross sections of Fe foam with short steel fibers after (a) 0, (b) 1, (c) 5, and (d) 10 redox cycles. Left column: low-magnification (1 mm scale) views, with epoxy mount background digitally filtered to enhance contrast. Right column: high-magnification (50 μm scale) views of representative lamellae with red arrows marking the Cr_2O_3-rich cores found within each lamella.

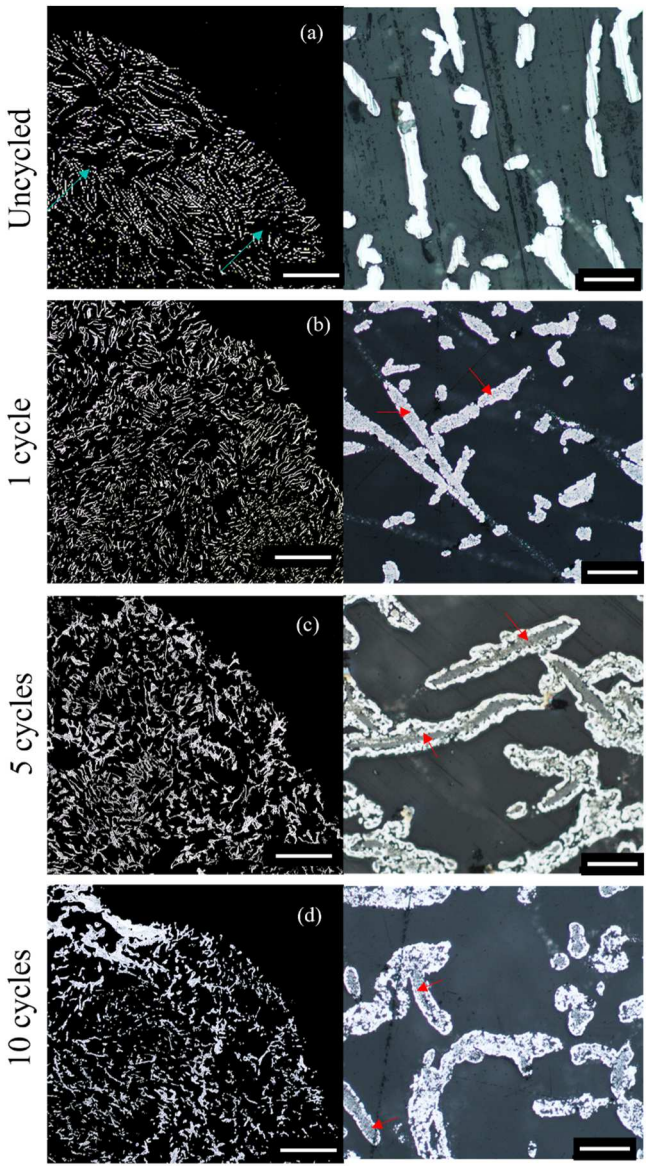

Fig. 8. Optical micrographs of radial cross sections of Fe foam with long steel fibers after (a) 0, (b) 1, (c) 5, and (d) 10 redox cycles. Left column: low-magnification (1 mm scale) views of ¼ of the foam cross-section; blue arrows mark large inter-colony gaps and epoxy mount background is digitally filtered to enhance contrast.. Right column: high-magnification (50 μm scale) views of representative lamellae, with red arrows marking Cr_2O_3-rich cores found within each lamella.

3.2.2. *Evolution of foams with short and long steel fibers*

The trends in Fig. 5 can be better understood by examining the microstructural and architectural evolution of each foam type. For steel-fiber foams, the interactions between the alloying additions from the stainless steel (Cr, Ni, Mn) and Fe from the freeze-cast lamellae strongly influences the resultant microstructure. Fig. 6 presents SEM micrographs for cross-sections of foams with short steel fibers after 0, 1, and 10 redox cycles, with corresponding EDS maps for Fe, Cr, and Ni, showing how these elements distribute across the lamellae and fibers. Because both steel fiber sizes have the same stainless steel composition (316 L), the results discussed here apply to the Fe foams with long steel fibers as well.

The as-sintered foam microstructure, shown in Fig. 6(a), consists of lamellae bridged by fibers. During sintering during the initial foam fabrication, the alloying elements present in the steel fibers (Cr, Ni, and Mn) diffuse into the Fe lamellae, resulting in a nominal uniform starting composition of Fe-2Cr-1Ni (at%) in the lamellae, as measured by EDS, which is consistent with the composition calculated assuming full homogenization between Fe lamellae and stainless-steel fibers. During the first oxidation redox half-cycle, Cr and minor amounts of Mn are expected to oxidize into Cr_2O_3 and MnO, which cannot be reduced by H_2 and thus remain stable during further redox cycling [39]. The presence of inert oxides (e.g., Cr_2O_3, ZrO_2, CeO_2) in Fe-based lamellar foams, added *ex-situ* during the freeze casting process, has previously been studied [33], with results similar to those observed here. In brief, the lack of adhesion between the oxide-rich lamellar core and the metal-rich lamellar shell induced internal delamination within lamellae, expanding their width and thus increasing the occurrence of contact between neighboring lamellae, followed by sintering of their Fe-rich shells.

Initially dispersed throughout the lamellae, the Cr_2O_3 particles formed during the first oxidation are rejected to the core of each lamella

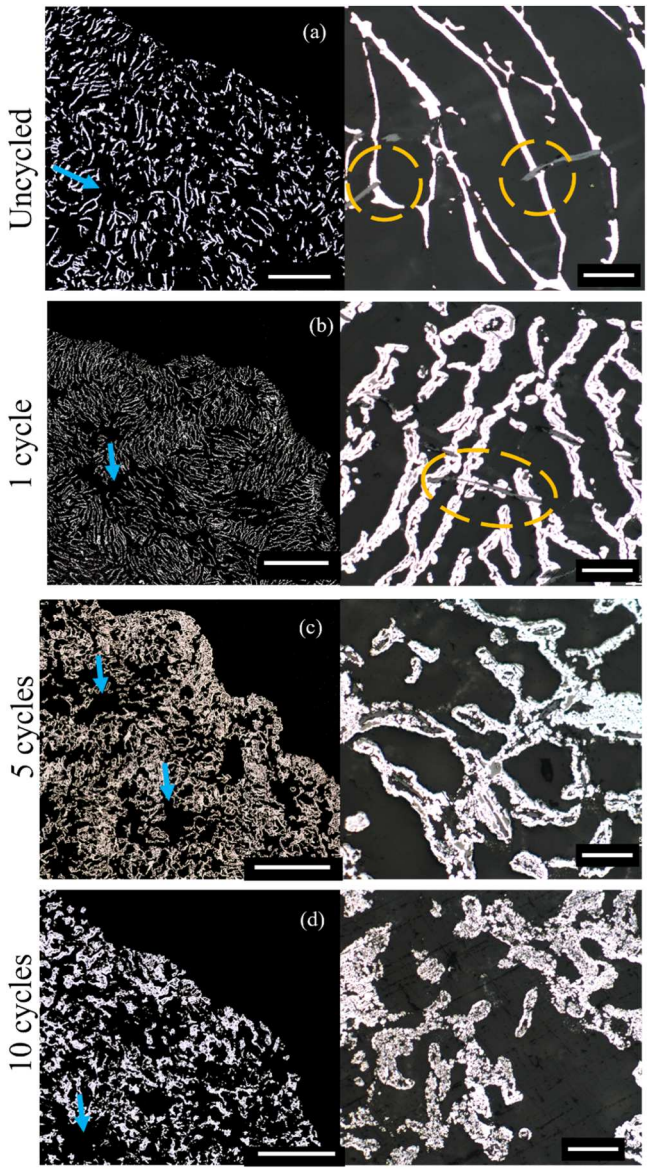

Fig. 9. Optical micrographs of radial cross sections of Fe foam with long YSZ fibers after (a) 0, (b) 1, (c) 5, and (d) 10 redox cycles. Left column: low-magnification (1 mm scale) views, with blue arrows pointing to large inter-colony gaps. Right column: high-magnification (50 μm scale) views of representative lamellae, with yellow ellipses showing fiber piercing lamellae in-plane.

during reduction and subsequent redox cycling, where they are surrounded by a Fe-1Ni shell. Iron continues to undergo reversible redox cycling, while Ni remains metallic [29,31]. The Ni content may provide some local kinetic benefit during reduction, but overall the effect is expected to be small because the Ni volume fraction is low [29,31]. The adhesion between the Cr_2O_3-rich core and the Fe-1Ni shell is poor, and internal lamellar delamination is commonly observed, with an example indicated by the red arrow in Fig. 6(b). Further redox cycling increases the severity of delamination, so that delaminated lamellar shells buckle and contact with neighbors, due to the large volume-change stresses created during oxidation. Upon reduction, neighboring Fe_3O_4 shells in contact with each other do not return to their initial positions, rather they sinter into a single, thicker lamellae.

For the short steel-fiber foams, the architectural changes are presented in Fig. 7. Macrographs of representative foams at 0, 1, 5, and 10 cycles are shown, with corresponding micrographs showing local changes in lamellar structure. The microstructure initially consists of small colonies of aligned lamellae, which are bridged by the fibers. Due to the Ni, Cr and Mn homogenization discussed previously, both fibers and lamellae have a uniform composition.

As visible in Fig. 7(a), channel porosity, which is initially high, decreases to approach the channel porosity seen in pure Fe samples after 5 cycles. This rapid drop in porosity is due both to the formation of lamella-widening Cr_2O_3 cores (discussed above) and to the lower efficacy of short fibers. Since there is a lower proportion of type I bridges, and because the type I bridges have a smaller diameter (and thus buckle more easily), the short fibers are unable to prevent densification over multiple cycles. Foam densification and channel closure result in iron oxide regions found deep within these thicker lamellae, which remain unreduced during the 90 min long reduction half-cycle. Longer reduction times could eventually reduce these buried oxide pockets, but as they grow larger with progressive lamellar densification, the reduction time becomes impracticably long, so the effective capacity of the material is reduced.

The microstructural evolution of foams with long and short steel fibers are quite similar to each other, but the overall morphology is very different due to the high initial channel porosity and channel thickness. Cyclic evolution of foam with long steel fibers is shown in Fig. 8 for foams uncycled and after 1, 5, and 10 cycles. As in the short steel fiber Fe foams (Fig. 7), the initial microstructure consists of small colonies of lamellae bridged by fibers, all with a uniform composition. The initial porosity is significantly higher than the short steel fiber Fe foams due to the increased efficacy of the fibers in preventing shrinkage during initial sintering after freeze casting. Some large inter-colony gaps are observed in this stage as well (blue arrows).

During cycling, the foams shrink and densify, albeit much less than the short steel fiber Fe foams. Some foam densification is due to the formation of Cr_2O_3 cores in each lamella (red arrows) leading to lamellar widening, thus increasing the occurrences of contact and sintering, as also observed in the short steel fiber Fe foams. Although local sintering occurs, the macroscopic sample porosity remains high, due to the large inter-colony gaps between locally densified regions. Lamellar buckling is also mitigated by the high proportion of type-I bridges. The large fiber length and diameter introduce a new mechanism for morphological change - fiber engulfment – which is not easily observed in the rapidly densifying short-fiber foams and is discussed in Section 3.2.4.

3.2.3. *Evolution of foams with long YSZ fibers*

In foams with long YSZ fibers, channel porosity is initially very high, similar to the foams with long steel fibers; the foam microstructural evolution is shown in Fig. 9 for foams after 0, 1,5, and 10 cycles. The microstructure initially consists of Fe lamellae bridged by YSZ fibers. There is no chemical interaction observed between the YSZ fibers and Fe lamellae, unlike in the foams with steel fibers. The lamellar colony structure resembles that of the foams with long steel fibers, with large inter-colony gaps present even before cycling (Fig. 9, blue arrows). The contact angle between the fiber and the lamellae is initially high (Fig. 9a, yellow circles) indicating a non-wetting, high energy surface, but in later cycles the Fe appears to wet the fibers. This effect, termed fiber engulfment, is explored in Section 3.2.4.

The lamellar colonies tend to be larger than those observed in either steel fiber Fe foams, but smaller than those observed in fiber-free Fe foams. As in the Fe foams with long steel fiber, the inter-colony gaps expand as individual colonies densify, because lamellae within each colony tend to buckle, contact, and sinter. The high initial porosity prevents extensive densification from occurring at the macroscopic foam level, but local densification is still prevalent as lamellae coalesce and densify within colonies.

YSZ fiber engulfment is also pronounced, as also observed in steel fiber foams, consistent with the large portion of type-I bridges (Fig. 4). During redox cycling, some of these type-I bridges are converted into type-III bridges via buckling and fracture, as shown in representative

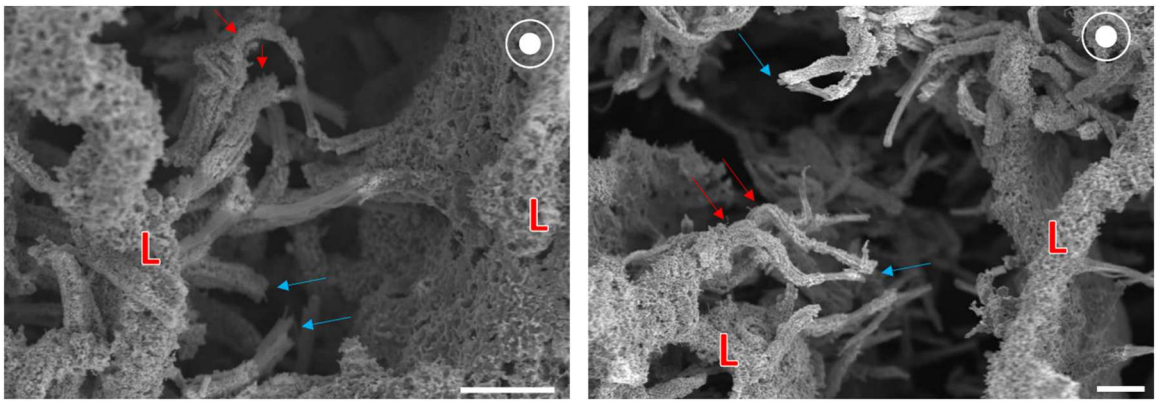

Fig. 10. SEM micrographs of Fe foam with long YSZ fibers after 5 redox cycles, showing YSZ fiber attached to Fe lamellae (marked with letter "L"), and subjected to buckling (red arrows) and fracture (blue arrows). Freeze cast direction indicated, scale bar marks 50 μm.

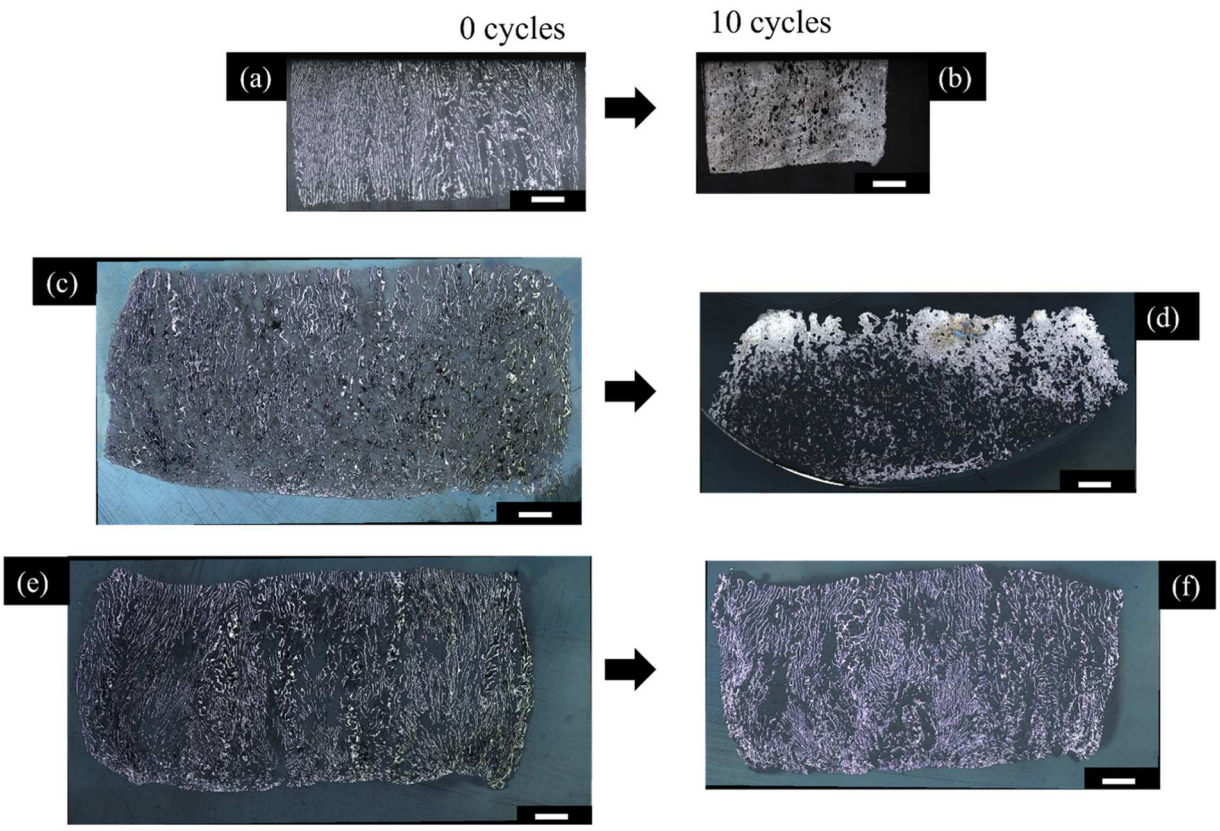

Fig. 11. Axial cross sections of foams with (a, b) short steel fibers, (c, d) long steel fibers, and (e, f) long YSZ fibers, after 0 (left column) and 10 right column) cycles. Solidification direction is vertical in all cases. All micrographs are to the same scale (scale bar: 1 mm) to illustrate foam shrinkage after cycling.

micrographs in Fig. 10.

In all cases, the lamellar structure is substantially densified after redox cycling. This is particularly apparent when viewing the freeze cast structures axially, as shown in Fig. 11. Although local densification occurs in the foam with long YSZ fibers, the overall porosity remains relatively high (Fig. 11e) as compared to the steel fiber foams (Fig. 11(b, d)). The anisotropy observed in shrinkage is also visible in Fig. 10: both long-fiber foams show axial shrinkage which is higher than radial shrinkage, consistent with radially-oriented fibers preventing sintering. For the short-fiber foam (Fig. 11b), radial shrinkage is larger, consistent with short fibers becoming ineffective after multiple redox cycles.

3.2.4. *Fiber engulfment mechanism*

All foams exhibit fiber engulfment, where Fe_3O_4 is cyclically deposited on the surface of the fibers and subsequently reduced to Fe. The morphological changes associated with this coarsening mechanism are best observed for long-fiber foams where lamellar densification is inhibited by the fibers. This process is depicted schematically in Fig. 12.

The foam colonies initially consist of distinct lamellae and fibers; for the steel fibers, the composition is homogenized after the initial sintering step, as Ni, Cr and Mn diffuse from fibers to the Fe lamellae (Fig. 12a). During the first oxidation half cycle (Fig. 12b), Fe_3O_4 grows on the lamellar surface and expands into the channels between lamellae, thus engulfing fibers. For the steel fibers, the first oxidation also creates a Cr_2O_3-rich lamellar core that remains present throughout further

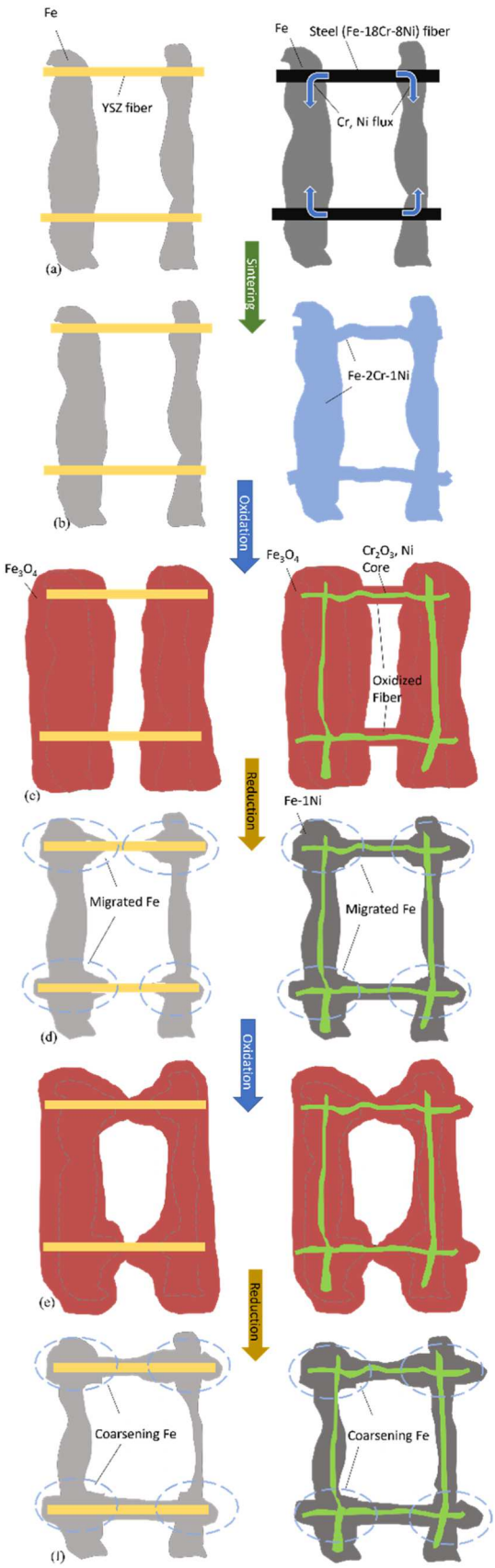

(caption on next column)

Fig. 12. Schematic cross-sectional depiction of fiber engulfment during redox cycling with (left column) YSZ fibers and (right column) steel fibers. (a) The initial microstructure shows two neighboring Fe lamellae bridged by fibers. For the steel fibers, the flux of the steel alloying elements which occurred during the powder sintering step is indicated by blue arrows. (b) During sintering, the foams with YSZ fibers do not undergo a chemical change, while those with steel fibers homogenize to a Fe-2Cr-1Ni composition. (c) During oxidation, the lamellae expand radially due to the molar volume increase between Fe and Fe_3O_4. For the foams with steel fibers, this oxidation also creates a Cr_2O_3-rich core that remains stable afterwards. The core also contains metallic Ni that is expected to rehomogenize with the Fe after reduction. (c) Upon reduction, the lamellar volume change is recovered, but a coating of reduced Fe remains on the fiber; as a result, over a full redox cycle, Fe is transferred from lamellae to fiber (blue circles). (d, e) Repeated redox cycling drives a continuously increasing engulfment of the fibers, and the coarsening of the coating Fe layer.

redox cycles; this core also contains Ni that is rejected during oxidation, and this Ni will rehomogenize with surrounding Fe during each reduction. During the first reduction half cycle (Fig. 12c), the lamellae shrink, thus liberating the fibers, but some reduced Fe remains on the surface the fiber; thus, at the end of the first redox cycle, some Fe has migrated from lamella to fiber (Fig. 12(c,e), blue circles). Each successive redox cycle pushes the engulfing Fe_3O_4 towards the center of the channel on oxidation and leaves Fe on the fiber on reduction, until the fiber is wholly engulfed. The mass flow is akin to a coarsening mechanism, first at the region near the intersection of the fiber and the lamella and then axially along the fiber, as Fe migrates. The driving force for this cyclical coarsening evolution is hypothesized to be a reduction of surface area, driving the transfer of Fe from the thicker planar lamellae to the thinner cylindrical fibers. This driving force appears to overcome the high surface energy suggested by the initially high contact angle between Fe lamellae and YSZ fibers shown in Fig. 9a.

For the steel fibers, the Cr_2O_3-rich core that forms during the first oxidation is analogous to the YSZ fibers: in both cases the geometry consists of an oxide core surrounded by a Fe shell, which undergoes redox cycling and further growth. Engulfment in the steel fibers is thus accelerated as compared to the YSZ fibers, since the steel fibers already have significant Fe content present before cycling begins. The behavior seen is analogous to what would be achieved by adding Cr_2O_3 fibers directly to Fe foams.

Fiber engulfment has an immediate effect on the microstructure and architecture of freeze-cast foams, as illustrated in Fig. 13. SEM micrographs of the same region of a long YSZ fiber foam after the first, second and third oxidation half-cycle are shown in Fig. 13(a–c), respectively. Although the original YSZ fiber surface can still be seen after the first half cycle, engulfment is clear near the intersections of fibers with lamellae. After the second oxidation, fibers are fully engulfed, but they can still be seen to bridge between lamellae as distinct features. After the third oxidation, however, fibers are no longer distinct from the lamellae. Instead, the structure has densified and coarsened significantly. Engulfed fibers, or engulfed fiber ends are marked with arrows.

Fig. 13(d) shows an axial cross section micrograph of a foam with long YSZ fibers after 5 redox cycles, with three representative fibers shown near a lamella. The YSZ cores of the fibers (red arrows) are distinguished from the Fe shell (yellow arrows) coating them: after 5 redox cycles, the initially 6 μm diameter bare YSZ fiber is engulfed in a shell quadrupling its diameter to ~25 μm.

Fig. 13(e,f) show engulfment in foams with long steel fibers after 5 redox cycles. The low magnification image in Fig. 11e illustrates the changing architecture of the foam: lamellae are no longer distinct, instead the coarsened fibers form a connected network. Fig. 13(f) shows a higher magnification image of the same foam, where again the initially 6 μm diameter fibers have coarsened to ~ 25 μm.

After 5 cycles, over 20% of the lamellar Fe volume has been transferred to the fibers, as determined by calculation of the engulfed fiber volume as compared to the initial lamellar volume in micro-tomographs.

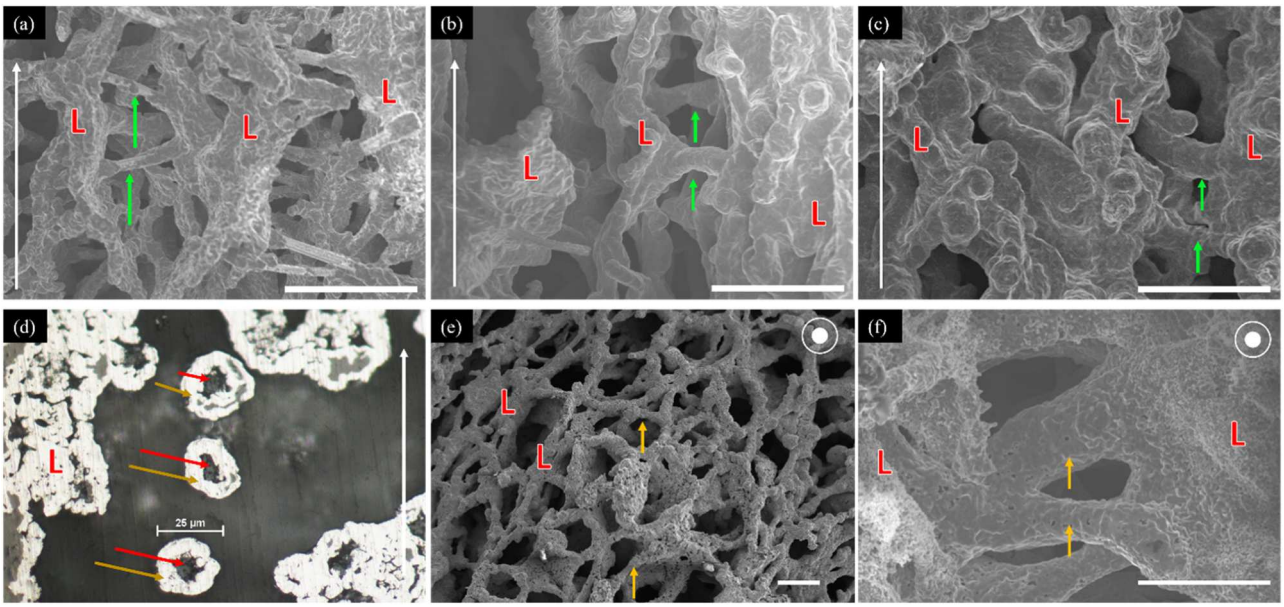

Fig. 13. Examples of fiber engulfment in SEM and optical micrographs: (a–c) SEM images of the same region in a foam (freeze cast direction indicated in white, scale bar marks 100 μm) with the same two long YSZ fibers (green arrows) bridging lamellae ("L"), after (a) 1, (b) 2, and (c) 3 oxidation half-cycles; (d) optical micrograph showing axial cross sections of three long YSZ fibers after 5 cycles, illustrating their Fe shell (yellow arrow) and YSZ core (red arrow). (e-f) low- and high-magnification SEM micrographs of foam with Fe-engulfed long steel fibers, after 5 redox cycles ("L" marks lamellae, yellow arrows mark fibers, freeze cast direction indicated in white, scale bar marks 100 μm).

The porosity of the foams remains relatively unchanged, even though areas of extensive local densification are observed at the intersection of multiple fibers in narrow channels. This transfer of Fe from lamellae to fibers changes the foam architecture, from its initial bridged lamellar state to a structure that more closely resembles a "bird's nest" architecture [40–42]. Local volumes with significant densification are present as well, which likely form in regions with some fiber aggregation where the coarsening of neighboring fibers leads to contact and sintering, as well as on the outer envelope of the foams where lamellar splitting results in accelerated densification [43]. These densified regions result in lost redox capacity over multiple cycles, indicating that the morphological shift from lamellar to mixed lamellar/fibrous degrades the sample with repeated redox cycling.

4. Conclusions

The effects of integrating fibers within lamellar Fe foams during freeze-casting are investigated, specifically for their effect on freeze-cast lamellar architecture and the evolution of that architecture as the foams undergo successive H_2–H_2O redox cycling at 800 °C between Fe and Fe_2O_3, with large volumetric changes. Three fiber types are investigated – stainless-steel fibers (short: 0.1 mm, and long: 1–2 mm) and YSZ fibers (long: 1–2 mm) – with a constant volume fraction of 15% with respect to Fe content of the foams. The following conclusions are drawn:

(1) Using a hybrid gel-freeze-casting method, long steel fibers can be distributed into a lamellar Fe foam without deleterious sedimentation. Foams show most (70%) long steel or YSZ fibers spanning channels fully, mostly normal to the growth direction and lamellar plane.
(2) Long fibers, both steel and YSZ, have a strong effect on the freeze-cast sample architecture by locally altering lamellar growth direction. This results in colonies of aligned lamellae being further apart from each other.
(3) All fiber types inhibit foam shrinkage during initial reduction and sintering from Fe_2O_3 to Fe, though the effect is more pronounced for the long fibers. This indicates that fibers are initially mechanically reinforcing the foams as intended, and macroscopic sintering shrinkage is mitigated by partial prevention of the lamellar buckling observed in fiber-free Fe foams.
(4) During redox cycling, the short steel fibers quickly lose efficacy owing to their smaller diameter and reduced ability to fully bridge channels. As a result, after only 5 redox cycles, the porosity of short-fiber and fiber-free foams are similar, and they then decrease further at the same rates.
(5) During redox cycling, long fibers prevent lamellar buckling but slowly lose efficacy due to fiber engulfment by Fe/Fe_2O_3 during cyclical redox volumetric changes. This engulfment alters the foam architecture, from an initial bridged lamellar state to a mixed lamellar/fibrous architecture, as Fe is transferred from lamellae to fibers in a cyclical coarsening mechanism. As the fibers become engulfed in Fe and coarsen, lamellar regions densify and macroscopic foam porosity decreases.

Data availability

The raw/processed data required to reproduce these findings cannot be shared at this time as the data also forms part of an ongoing study.

Declaration of Competing Interest

DCD discloses a financial interest in Cell Mobility, Inc., which is commercializing freeze-cast metal foams.

David Dunand reports financial support was provided by National Science Foundation. David Dunand reports a relationship with Cell Mobility Inc that includes: consulting or advisory and equity or stocks.

Acknowledgments

This research was funded by U.S. National Science Foundation (2015641). This research made use of the MatCI Facility supported by the MRSEC program of the National Science Foundation (DMR-1720139) at NU's Materials Research Center. It also used resources of the Advanced Photon Source (APS), a U.S. Department of Energy (DOE)

Office of Science user facility operated for the DOE Office of Science by Argonne National Laboratory under Contract No. DE-AC02-06CH11357. The authors thank Dr. Denis Keane and Dr. William Guise (APS) for collecting microtomographic data and assistance with tomographic reconstructions and Mr. Jacob Mack (NU) for useful discussions. The authors acknowledge Bekaert, Inc., Stanford Advanced Materials, and Zircar Zirconia for providing fiber samples for this research.

Supplementary materials

Supplementary material associated with this article can be found, in the online version, at doi:10.1016/j.actamat.2022.118543.

References

[1] K.L. Scotti, D.C. Dunand, Freeze casting – a review of processing, microstructure and properties via the open data repository, FreezeCasting.net, Prog. Mater Sci. 94 (2018) 243–305.
[2] E. Munch, E. Saiz, A.P. Tomsia, S. Deville, Architectural control of freeze-cast ceramics through additives and templating, J. Am. Ceram. Soc. 92 (7) (2009) 1534–1539.
[3] J. Pötschke, V. Rogge, On the behaviour of foreign particles at an advancing solid-liquid interface, J. Cryst. Growth 94 (3) (1989) 726–738.
[4] L. Qian, A. Ahmed, A. Foster, S.P. Rannard, A.I. Cooper, H. Zhang, Systematic tuning of pore morphologies and pore volumes in macroporous materials by freezing, J. Mater. Chem. 19 (29) (2009) 5212–5219.
[5] J.W. Moon, H.J. Hwang, M. Awano, K. Maeda, Preparation of NiO–YSZ tubular support with radially aligned pore channels, Mater. Lett. 57 (8) (2003) 1428–1434.
[6] T.L. Cable, S.W. Sofie, A symmetrical, planar SOFC design for NASA's high specific power density requirements, J. Power Sources 174 (1) (2007) 221–227.
[7] T. Wu, W. Zhang, B. Yu, J. Chen, A novel electrolyte-electrode interface structure with directional micro-channel fabricated by freeze casting: a minireview, Int. J. Hydrog. Energy 42 (50) (2017) 29900–29910.
[8] W. Dang, W. Wang, P. Wu, F. Li, K. Zhao, Y. Tang, Freeze-cast porous Al2O3 ceramics strengthened by up to 80% ceramics fibers, Ceram. Int. 48 (7) (2022) 9835–9841.
[9] X. Hu, L. Yang, L. Li, D. Xie, H. Du, Freeze casting of composite system with stable fiber network and movable particles, J. Eur. Ceram. Soc. 36 (16) (2016) 4147–4153.
[10] F. Li, T. Jia, W. Dang, Z. Xu, K. Zhao, Y. Tang, Porous Ti6Al4V alloys with high strength-to-modulus ratio fabricated by unidirectional freeze casting of SiC fiber-containing slurry, Mater. Sci. Eng. A 820 (2021), 141584.
[11] S. Roy, J. Gibmeier, K.A. Weidenmann, A. Wanner, Mechanical properties of innovative metal/ceramic composites based on freeze-cast ceramic preforms, in: T. Böllinghaus, J. Lexow, T. Kishi, M. Kitagawa (Eds.), Materials Challenges and Testing for Supply of Energy and Resources, Springer Berlin Heidelberg, Berlin, Heidelberg, 2012, pp. 213–220.
[12] C. Peko, B. Groth, I. Nettleship, The effect of polyvinyl alcohol on the microstructure and permeability of freeze-cast alumina, J. Am. Ceram. Soc. 93 (1) (2010) 115–120.
[13] M.N. Rahaman, Q. Fu, Manipulation of porous bioceramic microstructures by freezing of suspensions containing binary mixtures of solvents, J. Am. Ceram. Soc. 91 (12) (2008) 4137–4140.
[14] Q. Fu, M.N. Rahaman, F. Dogan, B.S. Bal, Freeze-cast hydroxyapatite scaffolds for bone tissue engineering applications, Biomed. Mater. 3 (2) (2008), 025005.
[15] Y. Zhang, L. Hu, J. Han, Z. Jiang, Freeze casting of aqueous alumina slurries with glycerol for porous ceramics, Ceram. Int. 36 (2) (2010) 617–621.
[16] S. Sabat, S. Sikder, S.K. Behera, A. Paul, Effect of freezing velocity and platelet size on structural parameters and morphology of freeze-cast porous alumina scaffolds, Ceram. Int. 47 (12) (2021) 16661–16673.
[17] C.D. Bohn, J.P. Cleeton, C.R. Müller, S.Y. Chuang, S.A. Scott, J.S. Dennis, Stabilizing iron oxide used in cycles of reduction and oxidation for hydrogen production, Energy Fuels 24 (7) (2010) 4025–4033.
[18] N. Xu, X. Li, X. Zhao, J.B. Goodenough, K. Huang, A novel solid oxide redox flow battery for grid energy storage, Energy Environ. Sci. 4 (12) (2011) 4942–4946.
[19] C.J. Zhang, K. Huang, A Comprehensive review on the development of solid-state metal-air batteries operated on oxide-ion chemistry, Adv. Energy Mater. 11 (2) (2021).
[20] X. Zhao, Y. Gong, X. Li, N. Xu, K. Huang, Cyclic Durability of a solid oxide Fe-air redox battery operated at 650°C, J. Electrochem. Soc. 160 (10) (2013) A1716–A1719.
[21] X. Zhao, Y. Gong, X. Li, N. Xu, K. Huang, Performance of solid oxide iron-air battery operated at 550 C, J. Electrochem. Soc. 160 (8) (2013) A1241.
[22] S.K. Wilke, D.C. Dunand, Structural evolution of directionally freeze-cast iron foams during oxidation/reduction cycles, Acta Mater. 162 (2019) 90–102.
[23] C.M. Berger, O. Tokariev, P. Orzessek, A. Hospach, Q. Fang, M. Bram, W. J. Quadakkers, N.H. Menzler, H.P. Buchkremer, Development of storage materials for high-temperature rechargeable oxide batteries, J. Energy Storage 1 (2015) 54–64.
[24] R.D. McKerracher, C.P. de Leon, R.G.A. Wills, A.A. Shah, F.C. Walsh, A review of the iron-air secondary battery for energy storage, ChemPlusChem 80 (2) (2015) 323. -+.
[25] C. Zhang, K. Huang, A comprehensive review on the development of solid-state metal–air batteries operated on oxide-ion chemistry, Adv. Energy Mater. 11 (2) (2021), 2000630.
[26] K. Otsuka, T. Kaburagi, C. Yamada, S. Takenaka, Chemical storage of hydrogen by modified iron oxides, J. Power Sources 122 (2) (2003) 111–121.
[27] Y. Saito, F. Kosaka, N. Kikuchi, H. Hatano, J. Otomo, Evaluation of microstructural changes and performance degradation in iron-based oxygen carriers during redox cycling for chemical looping systems with image analysis, Ind. Eng. Chem. Res. 57 (16) (2018) 5529–5538.
[28] R. Sepúlveda, A.A. Plunk, D.C. Dunand, Microstructure of Fe2O3 scaffolds created by freeze-casting and sintering, Mater. Lett. 142 (2015) 56–59.
[29] J.B. Mack, S.M. Pennell, D.C. Dunand, Microstructural evolution of lamellar Fe-25Ni foams during steam-hydrogen redox cycling, Acta Mater. 237 (2022), 118148.
[30] S.M. Pennell, J.B. Mack, D.C. Dunand, Evolution of lamellar architecture and microstructure during redox cycling of Fe-Co and Fe-Cu foams, J. Alloy. Compd. 918 (2022), 165606.
[31] S.K. Wilke, D.C. Dunand, Fe–Ni foams self-heal during redox cycling via reversible formation/homogenization of a ductile Ni scaffold, J. Mater. Chem. A 8 (37) (2020) 19375–19386.
[32] S.K. Wilke, D.C. Dunand, In operando tomography reveals degradation mechanisms in lamellar iron foams during redox cycling at 800°C, J. Power Sources 448 (2020), 227463.
[33] S.K. Wilke, R.A. Lundberg, D.C. Dunand, Hierarchical structural changes during redox cycling of Fe-based lamellar foams containing YSZ, CeO2, or ZrO2, ACS Appl. Mater. Interfaces 12 (24) (2020) 27190–27201.
[34] S.K. Wilke, J.B. Mack, C. Kenel, D.C. Dunand, Evolution of directionally freeze-cast Fe2O3 and Fe2O3+NiO green bodies during reduction and sintering to create lamellar Fe and Fe-20Ni foams, J. Alloy. Compd. 889 (2022), 161707.
[35] T. Um, S.K. Wilke, H. Choe, D.C. Dunand, Effects of pore morphology on the cyclical oxidation/reduction of iron foams created via camphene-based freeze casting, J. Alloy. Compd. 845 (2020), 156278.
[36] M.M. Porter, R. Imperio, M. Wen, M.A. Meyers, J. McKittrick, Bioinspired scaffolds with varying pore architectures and mechanical properties, Adv. Funct. Mater. 24 (14) (2014) 1978–1987.
[37] C. Stolze, T. Janoschka, U.S. Schubert, F.A. Müller, S. Flauder, Directional solidification with constant ice front velocity in the ice-templating process, Adv. Eng. Mater. 18 (1) (2016) 111–120.
[38] R. Dougherty, K.H. Kunzelmann, Computing local thickness of 3D structures with Imagej, Microsc. Microanal. 13 (S02) (2007) 1678–1679.
[39] M. Hasegawa, Chapter 3.3 - ellingham diagram, in: S. Seetharaman (Ed.), Treatise on Process Metallurgy, Elsevier, Boston, 2014, pp. 507–516.
[40] X. Dong, J. Liu, R. Hao, A. Guo, Z. Hou, M. Liu, High-temperature elasticity of fibrous ceramics with a bird's nest structure, J. Eur. Ceram. Soc. 33 (15) (2013) 3477–3481.
[41] X. Dong, G. Sui, J. Liu, A. Guo, S. Ren, M. Wang, H. Du, Mechanical behavior of fibrous ceramics with a bird's nest structure, Compos. Sci. Technol. 100 (2014) 92–98.
[42] F. He, W. Li, L. Zhou, L. Yang, H. Zhao, X. He, Preparation and characterization of the three-dimensional network mullite porous fibrous materials by pressure and freeze-casting method, Ceram. Int. 45 (3) (2019) 3954–3960.
[43] S.K. Wilke, D.C. Dunand, Finite element model for coupled diffusion and elastoplastic deformation during high-temperature oxidation of Fe to FeO, J. Electrochem. Soc. 167 (8) (2020), 080532.